

# Validation of FE Deformation Models using Ultrasonic and MR Images

Junji Muramatsu, Takashi Ikuta, Shinichi Hirai  
Dept. Robotics, Ritsumeikan Univ.  
Kusatsu, Shiga 525-8577, Japan

Shigehiro Morikawa  
Shiga University of Medical Science  
Otsu, Shiga 520-2192, Japan

**Abstract**—This paper describes the measurement of inner deformation of a rheological object using ultrasonic and MR images and comparison the measured and simulated deformations. We apply finite element (FE) model to simulate elastic, viscoplastic, and rheological deformation of soft objects. Ultrasonic and MR images are used to reveal the inner deformation of a soft object. Here we report the measurement and its evaluating by comparing measured and simulated deformations.

**Keywords**—simulation, measurement, FE model, ultrasonic images, MR images

## I. INTRODUCTION

Modeling of soft objects such as food dough and biological tissue is a current challenging issue in surgical simulation, human modeling, and food engineering. Physically-based modeling has been proposed in computer graphics to simulate the dynamic behavior of soft objects. This approach has been directly applied to surgical simulation and human modeling. Physical models are built in this approach to compute the deformation of soft objects. The deformed shapes were validated experimentally but the inner deformation has been out of focus because of the lack of sensing method. We have to validate the physical models by comparing the inner deformation of soft objects. In addition, most physical models are based on the assumption that the deformation is isotropic and uniform. Unfortunately, actual soft objects often do not follow this assumption. We should relax this assumption to build more realistic physical models. Here we have to measure the inner deformation of soft objects to build the realistic models.

We have developed the modeling and identification of rheologically deformable objects [1], [2] but the inner deformation has been out of scope. Recent progress in ultrasonography and three dimensional imaging such as CT and MRI is impressive [3], [4]. Using these technologies, we can measure the inner deformation of deformable soft objects for the validation of models as well as the modeling based on the inner deformation measurement. This paper describes the inner measurement of rheological object deformation and the comparison between the measured and simulated deformations.

## II. SIMULATION OF DYNAMIC DEFORMATION USING FE MODELS

a) *FE model of elastic object*: This section describes FE (Finite Element) model of elastic objects. In FE modeling,

an object is described by a set of triangles or tetrahedra. The object deformation is then formulated by the deformation of individual triangles or tetrahedra. In this section, we formulate planar deformation of an object of thickness  $h$ . The object is given by a set of triangles. Let  $T_p$  be one triangle, of which vertices are  $P_i, P_j$ , and  $P_k$ . Assume that  $P_i, P_j$ , and  $P_k$  follow the triangle  $T_p$  counterclockwise. Let  $[\xi_i, \eta_i]^T$  be the initial position of vertex  $P_i$ . Let  $S_p$  denotes the area of triangle  $T_p$  at its initial shape.

Let two-dimensional vector  $u_i$  denotes the displacement of vertex  $P_i$ . Deformation of triangle  $T_p$  is then described by the displacement of three vertices  $u_i, u_j$ , and  $u_k$ . Let  $f_i^p$  be an elastic force exerted at vertex  $P_i$  by the deformation of triangle  $T_p$ . Assuming that the elasticity is uniform and isotropic, the elastic deformation is characterized by Lamé's constants  $\lambda$  and  $\mu$ . Note that Lamé's constants are described by Young's modulus  $E$  and Poisson ratio  $\nu$  as follows:

$$\lambda = \frac{\nu E}{(1 + \nu)(1 - 2\nu)}, \quad \mu = \frac{E}{2(1 + \nu)}. \quad (1)$$

The deformation of triangle  $T_p$  yields a set of elastic forces exerted at its vertices:

$$\begin{bmatrix} f_i^p \\ f_j^p \\ f_k^p \end{bmatrix} = K_p \begin{bmatrix} u_i \\ u_j \\ u_k \end{bmatrix}. \quad (2)$$

Partial elastic matrix  $K_p$  is given by  $\lambda J_p^\lambda + \mu J_p^\mu$ , where  $J_p^\lambda$  and  $J_p^\mu$  are partial connection matrices given as follows:

$$J_p^\lambda = \frac{h}{4S_p} \begin{bmatrix} A_{j,k;j,k} & A_{j,k;k,i} & A_{j,k;i,j} \\ A_{k,i;i,j,k} & A_{k,i;k,i} & A_{k,i;i,j} \\ A_{i,j;j,j,k} & A_{i,j;k,i} & A_{i,j;i,j} \end{bmatrix} \quad (3)$$

$$J_p^\mu = \frac{h}{4S_p} \begin{bmatrix} 2B_{j,k;j,k} & 2B_{j,k;k,i} & 2B_{j,k;i,j} \\ 2B_{k,i;i,j,k} & 2B_{k,i;k,i} & 2B_{k,i;i,j} \\ 2B_{i,j;j,j,k} & 2B_{i,j;k,i} & 2B_{i,j;i,j} \end{bmatrix} + \frac{h}{4S_p} \begin{bmatrix} C_{j,k;j,k} & C_{j,k;k,i} & C_{j,k;i,j} \\ C_{k,i;i,j,k} & C_{k,i;k,i} & C_{k,i;i,j} \\ C_{i,j;j,j,k} & C_{i,j;k,i} & C_{i,j;i,j} \end{bmatrix}. \quad (4)$$

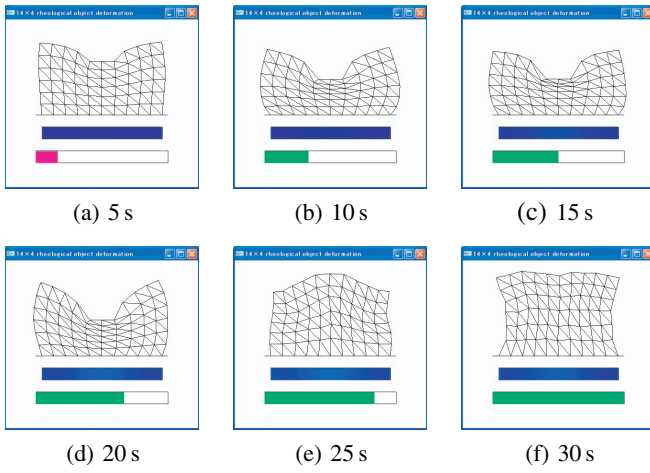


Fig. 1. Simulation of elastic deformation

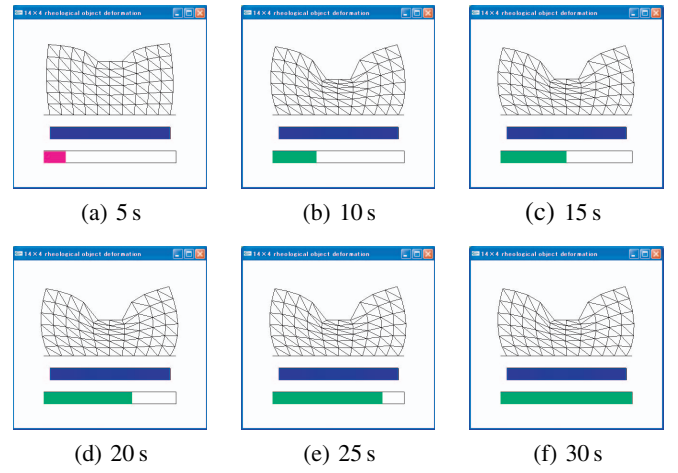


Fig. 2. Simulation of viscoplastic deformation

where

$$A_{i,j;l,m} = \begin{bmatrix} (\eta_i - \eta_j)(\eta_l - \eta_m) & -(\eta_i - \eta_j)(\xi_l - \xi_m) \\ -(\xi_i - \xi_j)(\eta_l - \eta_m) & (\xi_i - \xi_j)(\xi_l - \xi_m) \end{bmatrix},$$

$$B_{i,j;l,m} = \begin{bmatrix} (\eta_i - \eta_j)(\eta_l - \eta_m) & 0 \\ 0 & (\xi_i - \xi_j)(\xi_l - \xi_m) \end{bmatrix},$$

$$C_{i,j;l,m} = \begin{bmatrix} (\xi_i - \xi_j)(\xi_l - \xi_m) & -(\xi_i - \xi_j)(\eta_l - \eta_m) \\ -(\eta_i - \eta_j)(\xi_l - \xi_m) & (\eta_i - \eta_j)(\eta_l - \eta_m) \end{bmatrix}.$$

Let  $\mathbf{f}_i$  be a resultant elastic force at nodal point  $P_i$ . The resultant force  $\mathbf{f}_i$  is given by the sum of elastic forces caused by the deformation of triangles involving nodal point  $P_i$ :

$$\mathbf{f}_i = \sum_{\text{triangle } T_p \text{ involving vertex } P_i} \mathbf{f}_i^p. \quad (5)$$

Let  $\mathbf{u}_N$  be a collective vector consisting of displacement vectors at individual nodal points. A set of elastic forces at individual nodal points is then collectively described as  $-K\mathbf{u}_N$ . Elastic matrix  $K$  can be constructed from partial elastic matrices  $K_p$ .

Assuming that mass of a triangle equally concentrates to its three vertices, inertia matrix  $M_p$  of triangle  $T_p$  is given by a block diagonal matrix as follows:

$$M_p = \frac{\rho h S_p}{3} \begin{bmatrix} I_{2 \times 2} & O_{2 \times 2} & O_{2 \times 2} \\ O_{2 \times 2} & I_{2 \times 2} & O_{2 \times 2} \\ O_{2 \times 2} & O_{2 \times 2} & I_{2 \times 2} \end{bmatrix}. \quad (6)$$

Inertia matrix  $M$  of the object can be constructed from partial inertia matrices  $M_p$ .

In this section, we assume that an object deforms on the floor, implying that we should incorporate a geometric constraint caused by the floor. We apply Constraint Stabilization Method (CSM) to take the constraint into consideration. Let a geometric constraint be  $A^T \mathbf{u}_N = 0$ , where matrix  $A$  selects nodal points on which the constraint is imposed. Equation of motion of the constrained nodal points is collectively given by

$$A^T \ddot{\mathbf{u}}_N + A^T (2\omega \dot{\mathbf{u}}_N + \omega^2 \mathbf{u}_N) = \mathbf{0}. \quad (7)$$

Introducing a set of Lagrange's multipliers  $\lambda$ , which corresponds to a set of constraint forces, a set of equations of motion of individual nodal points on the object is described as follows:

$$-K\mathbf{u}_N + \mathbf{f} + A\lambda - M\ddot{\mathbf{u}}_N = \mathbf{0}, \quad (8)$$

where  $\mathbf{f}$  denotes a set of external forces applied to individual nodal points. Introducing nodal velocity vector  $\mathbf{v}_N = \dot{\mathbf{u}}_N$ , we have a set of differential equations of the first order:

$$\begin{bmatrix} I & & \\ & M & -A \\ & -A^T & \end{bmatrix} \begin{bmatrix} \dot{\mathbf{u}}_N \\ \dot{\mathbf{v}}_N \\ \lambda \end{bmatrix} = \begin{bmatrix} \mathbf{v}_N \\ -K\mathbf{u}_N + \mathbf{f} \\ A^T (2\omega \mathbf{v}_N + \omega^2 \mathbf{u}_N) \end{bmatrix}. \quad (9)$$

Giving the values of state variables  $\mathbf{u}_N$  and  $\mathbf{v}_N$ , we can compute the coefficient matrix on the left and the vector on the right. Since the coefficient matrix is regular, we can numerically compute  $\dot{\mathbf{u}}_N$  and  $\dot{\mathbf{v}}_N$ . Thus, applying numerical integration such as Runge-Kutta method, we can numerically compute the displacement and velocity of individual nodal points, resulting that we can compute the deformation of the object.

Fig. 1 shows a simulation result of an elastic object deforming. An elastic object is fixed on the floor. Simulation time is 30 s. The center of the top face is pushed down during the first 0 s, the displacement is kept during the next 10 s, and then the constraint is released. The density of the object is  $\rho = 6.4$  and its thickness is  $h = 1.0$ . The Young's modulus is  $E = 10$  and Poisson ratio is  $\nu = 0.35$ .

*b) FE model of viscoplastic object:* Viscoplastic deformation can be formulated by Maxwell model, which is a serial connection of an elastic element and a viscous element. Deformation remains after an applied force is released. A set of viscoplastic forces caused by the deformation of a viscoplastic object is given by

$$J^\lambda \mathbf{w}^\lambda + J^\mu \mathbf{w}^\mu. \quad (10)$$

Connection matrices  $J^\lambda$  and  $J^\mu$  can be constructed from partial connection matrices  $J_p^\lambda$  and  $J_p^\mu$  at individual triangles.

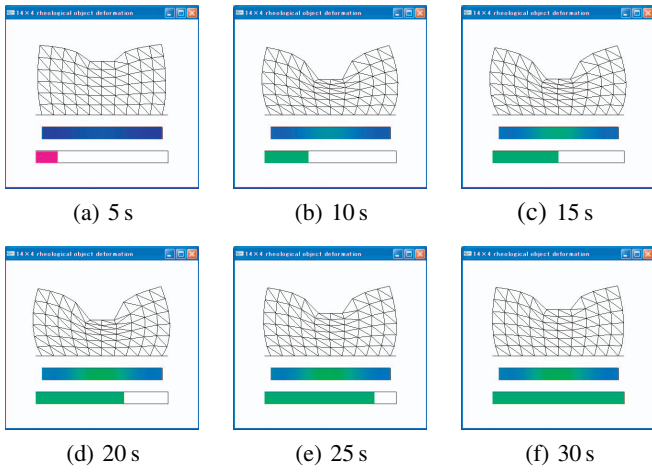


Fig. 3. Simulation of rheological deformation

Moreover, vector  $w^\lambda$  and  $w^\mu$  satisfy the following differential equations:

$$\dot{w}^\lambda = -\frac{\lambda^{\text{ela}}}{\lambda^{\text{vis}}} w^\lambda + \lambda^{\text{ela}} v_N, \quad (11)$$

$$\dot{w}^\mu = -\frac{\mu^{\text{ela}}}{\mu^{\text{vis}}} w^\mu + \mu^{\text{ela}} v_N. \quad (12)$$

Replacing a set of elastic forces  $-K u_N$  in the right side of eq.(9) by a set of viscoplastic forces  $-(J^\lambda w^\lambda + J^\mu w^\mu)$  and adding differential equations (11) and (12) yield a set of differential equations that describes viscoplastic deformation. Solving the obtained differential equations numerically, we can simulate the deformation of a viscoplastic object. Fig. 2 shows a simulation result of the deformation of a viscoplastic object. Viscoplastic parameters are  $E = 90$  and  $C = 50$ , Poisson's ratios are  $\nu^{\text{ela}} = \nu^{\text{vis}} = 0.35$ .

c) *FE model of rheological object*: Rheological deformation can be formulated by three-element model, which is a serial connection of a Voigt model and a viscous element. This element shows both viscoelastic deformation and plastic deformation. A set of rheological forces caused by the deformation of a rheological object is given by

$$(\lambda^{\text{vis}} J^\lambda + \mu^{\text{vis}} J^\mu) v_N + J^\lambda w^\lambda + J^\mu w^\mu. \quad (13)$$

Vector  $w^\lambda$  and  $w^\mu$  satisfy the following differential equations:

$$\dot{w}^\lambda = -\frac{\lambda^{\text{ela}}}{\lambda_1^{\text{vis}} + \lambda_2^{\text{vis}}} (w^\lambda - \lambda_2^{\text{vis}} v_N), \quad (14)$$

$$\dot{w}^\mu = -\frac{\mu^{\text{ela}}}{\mu_1^{\text{vis}} + \mu_2^{\text{vis}}} (w^\mu - \mu_2^{\text{vis}} v_N). \quad (15)$$

Parameters  $\lambda_1^{\text{vis}}$  and  $\mu_1^{\text{vis}}$  characterize the object viscosity while  $\lambda_2^{\text{vis}}$  and  $\mu_2^{\text{vis}}$  determine the object plasticity. Solving the differential equations numerically, we can simulate the deformation of a rheological object. Fig. 3 shows a simulation result of the deformation of a rheological object. Rheological parameters are  $E = 30$ ,  $C^{\text{ela}} = 200$ , and  $C^{\text{vis}} = 500$ , Poisson's ratios are  $\nu^{\text{ela}} = \nu_1^{\text{vis}} = \nu_2^{\text{vis}} = 0.35$ . The three-element model can describe viscoelastic, viscoplastic,

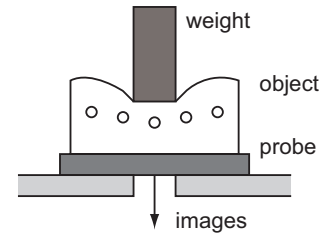


Fig. 4. Location of probe and object



Fig. 5. Example of ultrasonic image

and rheological deformations in a coherent manner. Actually, plastic deformation is described by letting  $E = 0$ . Letting  $C^{\text{vis}} = \infty$ , the model can describe viscoelastic deformation.

### III. MEASUREMENT OF INNER DEFORMATION VIA ULTRASONOGRAPHY

This section describes the sensing of inner deformation of a deformable object using ultrasonic imaging device. Ultrasonic waves are transmitted from a probe and the reflected waves are received at the probe. The received wave signals are sent to a computer to construct successive ultrasonic images from the signals. We have used a linear probe and B mode imaging, where the pixel value of an image corresponds to wave amplitude to measure the successive deformation of a cross-sectional plane. We have used Hitachi EUB-240. Resonance frequency of the probe is 3.5 MHz, frame rate is 24.6 Hz, and the resolution of images is  $320 \times 240$  pixels. We assumed that sound travels at its standard speed in tissue 1530 m/s.

A probe is set below a target object as shown in Fig. 4 so that the probe be in contact with the object to measure its inner deformation. The target object is made of agar consisting of carrageenan and locust bean gum. Carrageenan is a polysaccharide extracted from seaweeds. Locust bean gum is a galactomannan extracted from Carob tree seeds. This agar shows rheological deformation. Since the agar contains much water, we can obtain distinct ultrasonic images of the target object deformation. We used agar of concentration 5.0%.

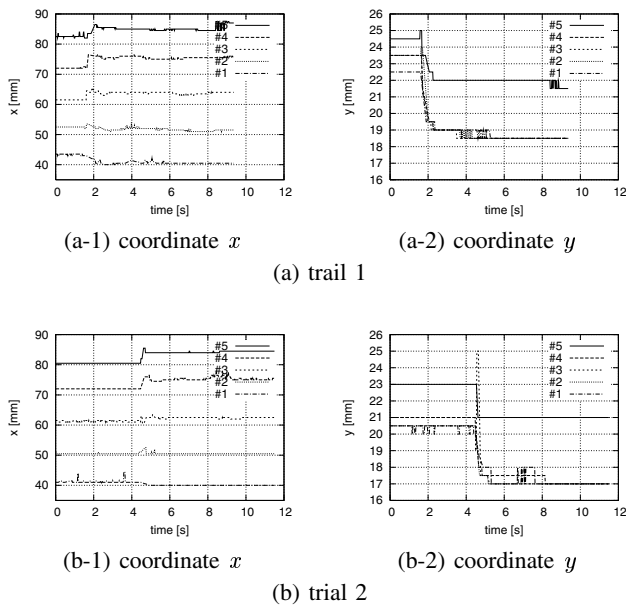


Fig. 6. Position of markers detected by ultrasonic images

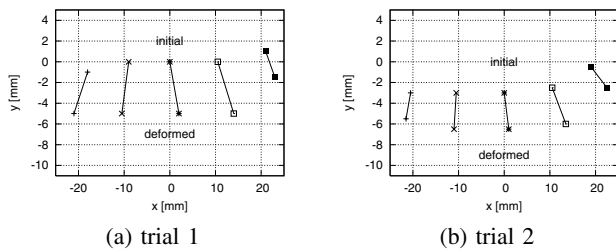


Fig. 7. Position of markers in initial and deformed shapes

The target object is a rectangular parallelepiped of which top surface is a square of 75 mm length and height is 30 mm. The object weighs 200 g. We inserted five markers along the central cross-sectional plane of the object with the interval of 10 mm. Let us put a cylindrical weight of weight 500 g and diameter 40 mm on the center of the object to surface to deform the object. A measured deformation is shown in Fig. 5. We find five markers at the bottom of the image and the object surface above the markers. Additionally, we find ghosts of markers and the surface above. Positions of markers are computed by processing measured images. We specify a processing region in images to eliminate the ghosts. We can compute the displacements of markers from images before and after deformation. The humidity was 34 % and the temperature was 26 °C. Temperature of the object surface was 23 °C.

Fig. 6-(a) and Fig. 6-(b) show the first and the second measurement results. We assumed that the initial position of the middle marker be the origin of the coordinate system. We have eliminated extraordinary measured values comparing the actual deformation, resulting the lack of values. Table I summarizes the measured values at the initial shape and at the deformed shape after 6 s. The values are plotted in Fig. 7.

TABLE I

MARKER COORDINATES IN INITIAL AND DEFORMED SHAPES DETECTED BY ULTRASONIC IMAGES (MM)

trial 1		
marker	initial shape	deformed shape
#1	( -18.0, -1.0 )	( -21.0, -5.0 )
#2	( -9.0, 0.0 )	( -10.5, -5.0 )
#3	( 0.0, 0.0 )	( 2.0, -5.0 )
#4	( 10.5, 0.0 )	( 14.0, -5.0 )
#5	( 21.0, 1.0 )	( 23.0, -1.5 )
trial 2		
marker	initial shape	deformed shape
#1	( -20.5, -3.0 )	( -21.5, -5.5 )
#2	( -10.5, -3.0 )	( -11.0, -6.5 )
#3	( 0.0, -3.0 )	( 1.0, -6.5 )
#4	( 10.5, -2.5 )	( 13.5, -6.0 )
#5	( 19.0, -0.5 )	( 22.5, -2.5 )

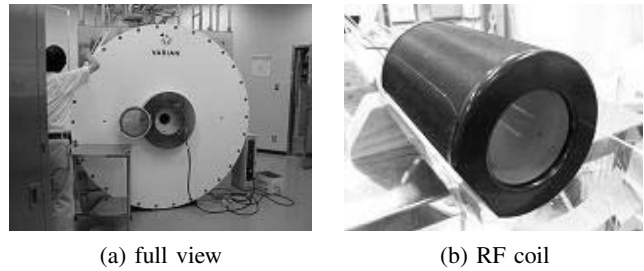


Fig. 8. MRI device

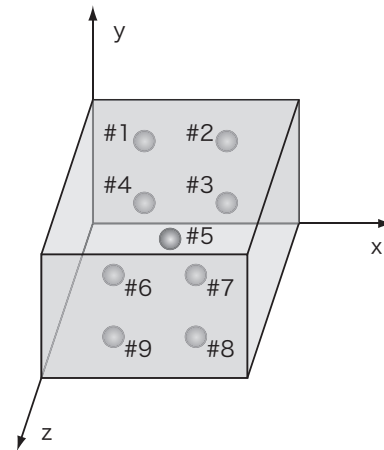


Fig. 9. Location of markers in MR imaging

#### IV. MEASUREMENT OF INNER DEFORMATION VIA MR IMAGING

An MRI device measures cross-sectional images of a target object and obtain a three-dimensional image by constructing the cross-sectional images. Cross-sectional images are referred to as slice images and the interval between two slice images is referred to as slice interval. MR imaging enables us to detect a cross-sectional image along any plane and to measure three-dimensional deformation inside an object. Unfortunately, it takes much time to obtain a three-dimensional image, making it difficult to capture dynamic deformation of an object. We have used a MRI device shown in Fig. 8-(a), which is installed at Shiga University of Medical Science. A target object is fixed

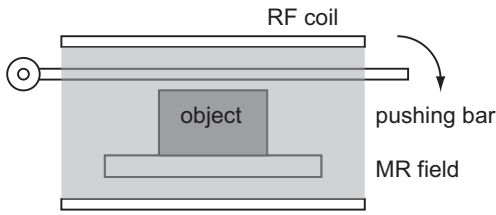


Fig. 10. Setup in MR imaging

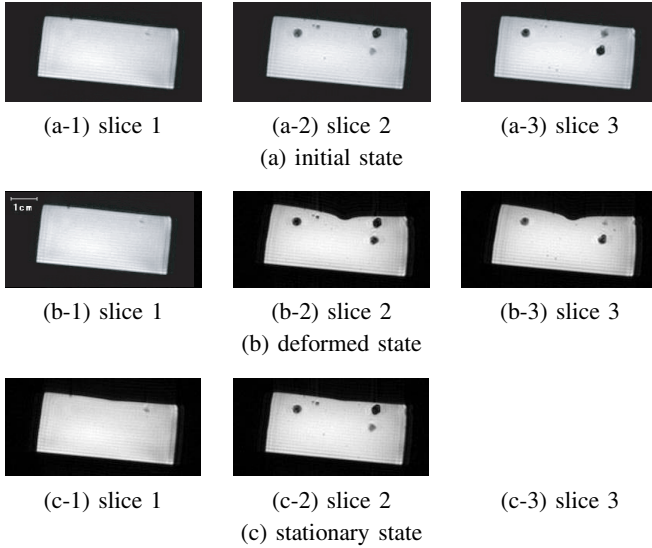


Fig. 11. MR images at initial, deformed, and stationary states

inside of an RF coil, shown in Fig. 8-(b), before the coil is inserted into the device for the measurement.

The inner diameter of an RF coil used in our experiment is 63 mm. A target object of width 55 mm, depth 55 mm, and height 25 mm made of agar on an acrylic plate of width 55 mm and thickness 2 mm is inserted into the coil. Plastic beads of diameter 2 mm are inserted in the target object as markers. The location of the markers is illustrated in Fig. 9. Gadolinium medium is mixed with agar to emphasize the image contrast.

TABLE II

MARKER COORDINATES AT INITIAL, DEFORMED, AND STATIONARY STATES DETECTED BY MR IMAGES (MM)

marker	initial state	deformed state	stationary state
#1	(12, 21, 11)	(12, 21, 11)	(12, 21, 11)
#2	(45, 25, 10)	(41, 24, 10)	(46, 24, 10)
#3	(45, 17, 12)	(41, 16, 11)	(45, 16, 12)
#4	(17, 24, 18)	(18, 24, 17)	(17, 24, 17)
#5	(25, 20, 28)	(25, 18, 27)	(25, 20, 27)
#6	(12, 21, 42)	(12, 21, 42)	(11, 21, 42)
#7	(44, 27, 43)	(45, 24, 44)	(44, 26, 43)
#8	(45, 17, 43)	(47, 16, 43)	(45, 16, 43)
#9	(11, 7, 44)	(11, 7, 44)	(11, 7, 43)

An acrylic cylindrical bar of diameter 20 mm is through the coil. One end is fixed and the other end is pushed down manually to deform a target object below the bar, as shown in Fig. 10. The bar is along the  $z$ -axis denoted in Fig. 9. We have applied two measurements. The first measurement is three-

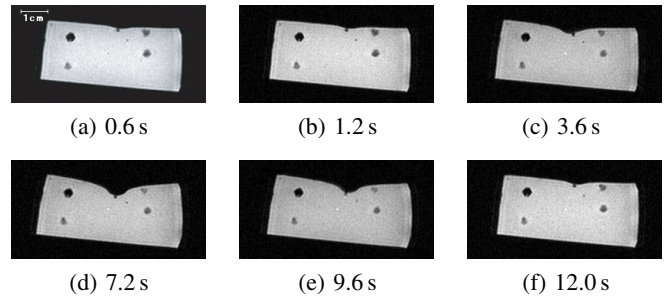


Fig. 12. Successive images of one cross-section

dimensional and static while the second measurement is two-dimensional and dynamic. In the first measurement, the MRI device obtains the successive three-dimensional images of slice interval 2 mm. The initial shape where no external forces are applied to the object, the deformed shape where the bar is pushed down, and the relaxed shape after the applied forces are released away are measured with enough time intervals. In the second measurement, the MRI device obtains successive images of one cross-sectional plane. The bar is pushed down and is released back dynamically.

The result of the first measurement is shown in Fig. 11. We obtained a set of 30 slice images with slice interval 2 mm. The figure shows successive 3 slices of the 30 images. Fig. 11-(a) through (c) correspond to the initial shape, Fig. 11-(d) through (f) correspond to the deformed shape, and Fig. 11-(g) through (i) correspond to the relaxed shape. The position of markers can be computed from these images. Table II summarizes the computed position of 9 markers inside of a deforming agar object.

The result of the second measurement is shown in Fig. 12. Selecting one slice image where markers can be found and measuring the corresponding cross-sectional plane successively, we examined shorter time interval in the image measurement. We found that time interval of 0.6 s is possible, as shown in the figure. Decreasing the resolution of MR images, we can reduce the time interval more.

## V. EVALUATION

*d) Comparison between ultrasonic sound images and simulation results:* Let us examine FE models by comparing the inner deformation obtained from ultrasonic sound images and simulation results. We have five markers inside of an agar target object. We compare the displacements of the middle three markers, that are, markers #2, #3, and #4. The locations of markers in simulation are described by black circles in Fig. 13. We compute the displacements of markers at the stable deformed shape of the target object. Fig. 14 shows the measured and simulated displacements of the three markers. Fig. 14-(a) through (c) shows respectively the displacements of markers #2, #3, and #4. The solid lines correspond to a simulation result when the center of the top surface of the object is pushed down. The dotted lines correspond to a simulation result when a nodal point deviated from the center to the left side by one mesh is pushed down. Measured

## ACKNOWLEDGMENT

This research was supported by Grant in Aid for Scientific Research (17206024) by the Ministry of Education, Culture, Sports, Science and Technology of Japan.

## REFERENCES

- [1] Masafumi Kimura, Yuuta Sugiyama, Seiji Tomokuni, and Shinichi Hirai, *Constructing Rheologically Deformable Virtual Objects*, Proc. IEEE Int. Conf. on Robotics and Automation, pp.3737–3743, Taipei, September, 2003.
- [2] Naoki Ueda, Shinichi Hirai, and Hiromi T. Tanaka, *Extracting Rheological Properties of Deformable Objects with Haptic Vision*, Proc. IEEE Int. Conf. on Robotics and Automation, pp.3902–3907, New Orleans, April, 2004.
- [3] Frank G. Gress and Ishan Bhattacharya, *Endoscopic Ultrasonography*, Blackwell Publishers, 2001.
- [4] Donald W. McRobbie, Elizabeth A. Moore, Martin J. Graves, and Martin R. Prince, *MRI from Picture to Proton*, Cambridge University Press, 2002.

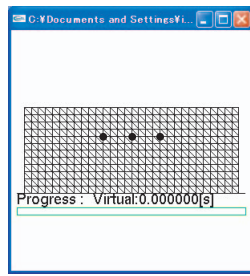


Fig. 13. Location of markers in simulation

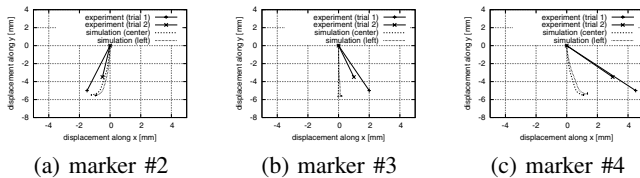


Fig. 14. Comparison between simulation and experiment

displacements from the initial locations to the stable locations are also plotted in the figure. As shown in Fig. 14-(b), the middle marker #3 moves downward but slightly in the right direction. This is caused by the location of the weight is biased to the right direction. Thus, we have computed the dotted lines. Let us compare this simulation with the first measurement. The errors between the measured and simulated results are as follows: 1.0 mm along  $x$ -axis and 0.5 mm along  $y$ -axis at marker #2, 1.8 mm along  $x$ -axis and 0.5 mm along  $y$ -axis at marker #3, and 2.8 mm along  $x$ -axis and 0.2 mm along  $y$ -axis at marker #4. We find that errors along  $x$ -axis is relatively large. Comparison with the second measurement also yields this tendency. This discrepancy comes from 1) errors in parameter identification, 2) nonlinearity or non-isotropic nature of deformation, and 3) non-uniform deformation, especially, difference between surface deformation and inner deformation.

*e) Comparison between MR images and simulation results:* As shown in Table II, marker #5 just under the acrylic pushing bar moves downwards along  $y$ -axis. In addition, the marker moves upwards along  $y$ -axis after the bar is pulled up. On the other side, displacements of other markers cannot be detected from the MR images. This may be caused by the pushing method we applied. We should reconsider how to deform a target object in the MRI device.

## VI. CONCLUSION

FE models developed in this paper can simulate the inner deformation of an agar object. But, the error along the horizontal axis is relatively large, which may come from nonlinearity or non-isotropic nature of deformation as well as non-uniform deformation, especially, difference between surface deformation and inner deformation. We are going to build FE models considering these properties. We have inserted artificial markers inside a target object to measure the inner deformation of the object. We are going to introduce tracking algorithms in computer vision to measure the inner deformation of actual biological objects.